www.acsnano.org

Silicon Nitride Nanopores Formed by Simple Chemical Etching: DNA Translocations and TEM Imaging

Zehui Xia,* Andre Scott, Rachael Keneipp, Joshua Chen, David J. Niedzwiecki, Brian DiPaolo, and Marija Drndić*



Downloaded via UNIV OF PENNSYLVANIA on May 22, 2023 at 20:48:39 (UTC). See https://pubs.acs.org/sharingguidelines for options on how to legitimately share published articles.

Cite This: ACS Nano 2022, 16, 18648-18657



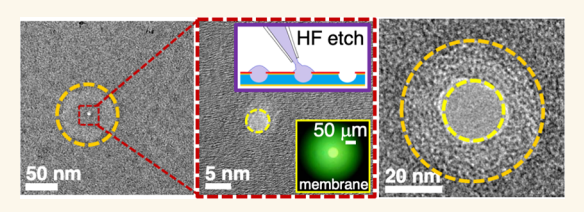
ACCESS

III Metrics & More

Article Recommendations

Supporting Information

ABSTRACT: We demonstrate DNA translocations through silicon nitride pores formed by simple chemical etching on glass substrates using microscopic amounts of hydrofluoric acid. DNA translocations and transmission electron microscopy (TEM) prove the fabrication of nanopores and allow their characterization. From ionic measurements on 318 chips, we report the effective pore diameters ranging from zero (pristine membranes) and sub-nm to over 100 nm, within 50 μ m



diameter membranes. The combination of ionic conductance, DNA current blockades, TEM imaging, and electron energy loss spectroscopy (EELS) provides comprehensive information about the pore area and number, from single to few pores, and pore structure. We also show the formation of thinned membrane regions as precursors of pores. The average pore density, about 5×10^{-4} pores/ μ m², allows pore number adjustment statistically (0, 1, or more). This simple and affordable chemical method for making solid-state nanopores accelerates their adoption for DNA sensing and characterization applications.

KEYWORDS: nanopore, fused silica (glass) chip, nanoporous membranes, silicon nitride, hydrofluoric acid, etching

henomena in solid-state pores have been studied over the past 20 years, particularly focused on ion transport and interactions in pores formed in silicon nitride (SiN_x) membranes.²⁻⁷ SiN_x membranes also facilitated many studies because of their standard microsystems processing, thermal stability, chemical inertness, and insulating properties. Numerous studies included SiN_x membranes as robust, high temperature supports for transmission electron microscopy⁸ (TEM) and X-ray diffraction, 10 as well as porous SiN_x membranes for imaging, fluidics, and molecule detection. 7,11 Formation of nanopores is typically performed using focused ion beam (FIB),² electron-beam lithography patterning,¹² TEM drilling,^{13,14} voltage application,¹⁵ and laser-assisted membrane poration. 16,17 Even when highly perforated with densely packed holes, SiNx membranes possess mechanical strength up to several bars of transmembrane pressure and withstand high temperatures up to 900 °C. 12 SiN_x membranes are inert to aggressive chemicals such as hot concentrated potassium hydroxide, piranha, and nitric acid, ¹² making them attractive in high resolution microscopy, 19 nanofluidics, 20,21 nanophotonics, 22,23 microelectromechanical systems (MEMS),^{24,25} and other fields.

Easy and simple manufacturing of small solid-state pores has been one of the long-standing challenges in the nanopore field. While TEM and FIB are considered expensive and difficult to scale up, electroporation is considered a cheaper alternative and still in development.²⁶ Finding easier ways of scalable and inexpensive nanopore manufacturing is of great importance for the acceleration and ultimate reach of this technology.

In this work, we report the discovery and characterization of a simple chemical method for SiN_x nanopore formation. This approach is based on microscopic hydrofluoric acid (HF) etching of the SiN_x membrane using a pipette-based HF processing method. We report the statistics on 318 chips, including nanopore sizes, and demonstrate DNA translocations through single nanopores made by etching. We show statistics of effective pore diameters as derived from ionic conductance and total porous area, from zero and sub-nm up to >100 nm. The pores are formed in 20 and 100 nm thick, ~50 μ m diameter SiN_x membranes on low-noise glass chips. $^{27-30}$ We analyzed 26 chips with TEM to further correlate ionic data and TEM. We prove that pore formation is induced by SiN_x exposure to μ L amounts of HF followed by water rinsing and drying. TEM analysis provides insights on pore sizes and

Received: July 21, 2022 Accepted: October 13, 2022 Published: October 17, 2022





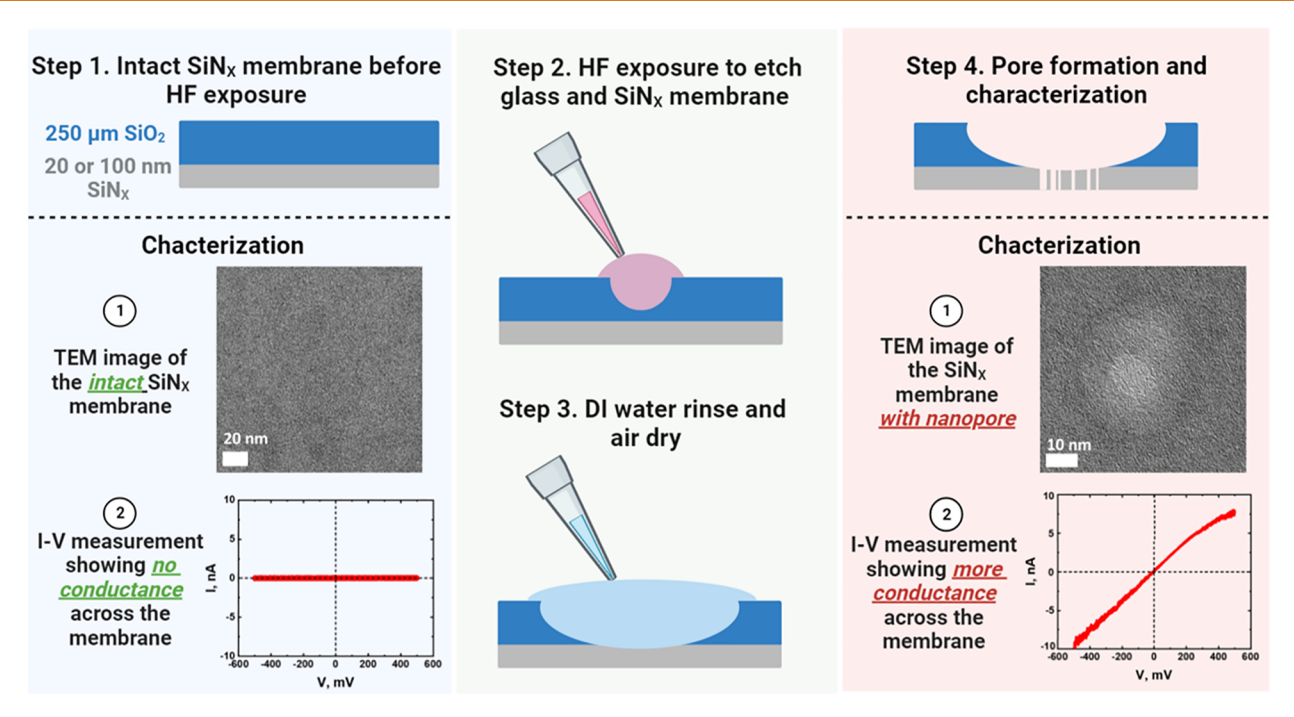


Figure 1. Schematic of SiN_x membrane HF-exposure and processing, pore formation, and characterization. (Step 1) Intact membranes show uniform surfaces and zero ionic conductance. Each chip contains one circular membrane of diameter of ~50 μ m. Note the sketches are not to scale. (Step 2) Membranes are etched in HF for a controlled time and then (step 3) rinsed in DI water. (Step 4) Membrane characterization is performed by TEM imaging and ionic current and DNA translocation measurements. Using TEM imaging, we observed up to about seven pores on a single membrane on glass chips. *Caution:* Proper safety procedures should be followed with HF. It is toxic and colorless.

statistics, while ionic current measurements characterize the total pore area. Given the known double-stranded DNA (dsDNA) diameter of 2.2 nm, DNA translocation recordings at high signal-to-noise and signal analysis confirm good quality of single pores and their diameter from the observed open pore currents, corroborating pore sizes measured by TEM. On a single SiN_x membrane on a glass chip, we located and imaged up to about seven pores using TEM. The average pore density, about 5×10^{-4} pores/ μ m², allows pore number adjustment statistically (0, 1, or more). Electron energy loss spectroscopy (EELS) in an aberration-corrected TEM provides twodimensional spatial elemental composition mappings that reveal the chemical structure of the nanopores under these specific experimental conditions. From EELS, we observed both N- and Si-deficient thinned regions around the nanopore. Thinned circular regions are interpreted as the precursors of pores, as confirmed by both TEM and EELS. This simple and affordable chemical method accelerates the adoption of solidstate nanopores for DNA sensing and characterization applications.

RESULTS AND DISCUSSION

Figure 1 shows the experimental workflow, steps 1–4, to form the etched SiN_x and characterize them via ionic measurements, TEM imaging, and DNA translocations. Procedures to fabricate suspended SiN_x membranes have been well documented previously, including procedures to make glass chips using patterning and chemical processing. Uniformity of SiN_x membranes is confirmed by both TEM imaging and background ionic conductance levels that fall within the noise of the measurement during ionic measurements, illustrated in step 1 (<0.01 nS, measured by the Nanopore Reader, Elements SRL, Figure S1 in Supporting

Information). The initial stoichiometry of these SiN_x membranes was determined using EELS,³² showing a ratio of $Si/N \approx 1.4$. In this work, however, the processing of glass chips is modified for membrane etching using small droplet quantities of HF acid, placed on each chip using a pipette (step 2). This ensures local etching and good etch-time control in chip processing. Specifically, 0.5 μ L of HF was administered to individual chips in a consecutive way for 5 s and then aspirated with a pipette (step 2). Five microliters of DI water was used to rinse each chip, and then this was pipette-aspirated twice as illustrated in the schematics (step 3). The chips were then left to air-dry after aspiration of the DI water and transported for further TEM imaging and ionic current characterizations and translocation measurements (step 4) to characterize pore formation and properties. In addition to glass chips, we used the typical Si chips³³ as controls to prove that pores form exclusively due to SiN_x exposure to HF. These Si chips are excellent control samples because their processing 13,31,34 uses different etchants to define the SiN, membrane (KOH for Si vs HF for SiO₂ chips). SiN_x membranes on Si chips are not exposed to HF during fabrication, while glass chips require HF to etch the SiO₂. 27,28 Hydrofluoric acid is introduced into the hemispheres in the glass chip to produce the final membrane whose size is a function of the etch depth and the starting thickness^{7,27,30} (Figure S6 in Supporting Information). The etch time is finely controlled to create thin membranes, and additional HF exposure is shown here to produce a statistically controlled number of small pores. We report results on chip measurements via current-voltage (I-V) testing in 1 M KCl as well as TEM imaging. Conclusions are drawn from testing the 318 chips. Specifically, Figure 6 summarizes the statistical findings.

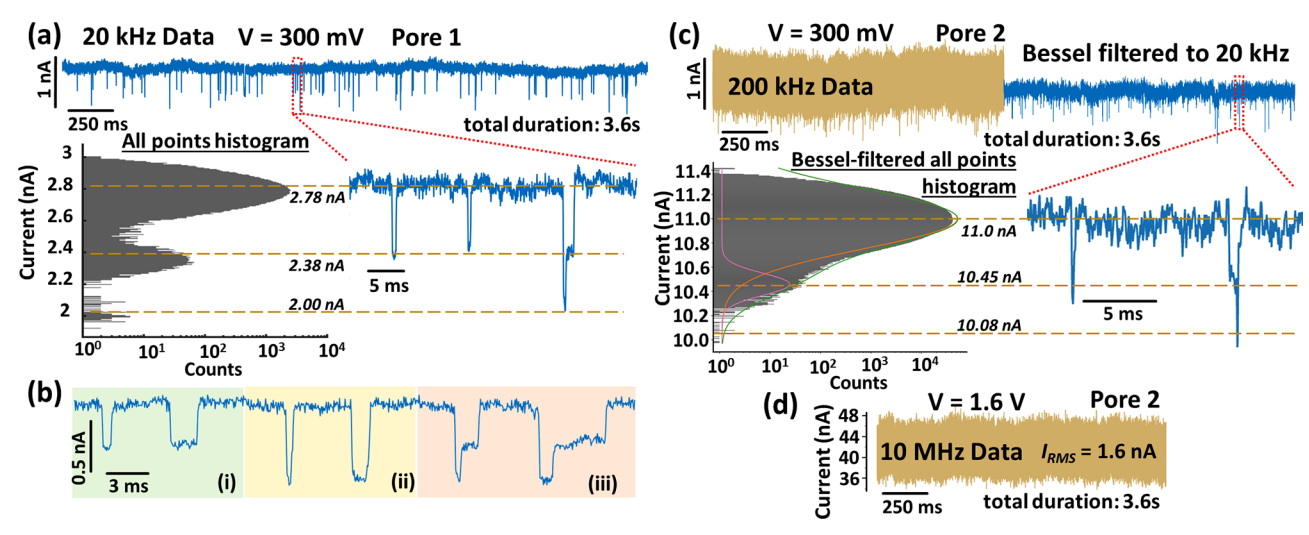


Figure 2. DNA translocations through HF-etched SiN_x nanopores in 1 M KCl. (a) Current vs time trace (3.6 s long) after addition of 1 kbp dsDNA at V=300 mV, all-points histogram, and zoom-in view on one section of the trace. The trace was recorded using a portable nanopore reader from Elements SRL, at 20 kHz bandwidth. ^{28,29,47} The calculated pore diameter from the open pore current is 4.8 nm assuming a thickness of 20 nm. Control measurements with no DNA showed no detectable translocations. (b) We detect only three types of events shown from (i) to (iii), where DNA is unfolded, fully folded, and partially folded, respectively. The agreement between G, ΔG (for unfolded DNA), and ΔG (for folded DNA) with the measured values provides evidence for single pore formation. (c) DNA translocations in 1 M KCl at V=300 mV were recorded at 200 kHz bandwidth using the portable 200 kHz nanopore reader from Elements SRL. A 20 kHz low-pass Bessel filter is applied to distinguish event characteristics against noise. Translocation event shapes are consistent with (a) and (b) with regard to folded and unfolded variety of events. (d) Current vs time trace (3.6 s long) of DNA translocation recorded at 10 MHz using another 10 MHz nanopore reader from Elements SRL. I_{RMS} value is indicated. No translocation events were detected, and further improvements of signal-to-noise are required for detection at this record high bandwidth.

Specifically, in this work we did not clean the nanopore chips with hot piranha or other methods in between the HF etching step to make the pores and their further characterization. Piranha cleaning might slightly etch the pore and induce pore diameter expansion, which can further interfere with the interpretation of the results by adding more variables. For samples in Figure 3c, we see a good match between diameters extracted from TEM and ionic measurements for samples with low G (one to few small pores identified by TEM imaging). Similarly, we were able to translocate DNA through these nanopores without piranha or other treatments. However, it is important to note that sample history and treatments can likely affect the comparison between ionic and TEM-extracted information, and errors introduced by specific experimental procedures should be carefully considered in practical applications. However, the match found here is quite consistent across samples, indicating that ionic and TEM measurements do provide consistent data under these experimental conditions. We also stress the possible errors introduced by using ionic currents to estimate pore sizes which assume uniform pore thicknesses. This is a strong assumption, but we do not have the experimental ability to measure individual nanopore thicknesses precisely. These thicknesses can be likely different from the surrounding membrane thickness (see derivation of eq 5).

Figure 2 shows ionic transport and DNA translocation data collected at a range of bandwidths of 20 kHz, 200 kHz, and 10 MHz through a few 20 nm SiN_x membranes processed as described (Figure 1). These measurements establish the presence of pores. Ionic current versus voltage, and dsDNA translocation signals were observed and characterized when constant voltage was applied and DNA was added. The fluctuating open pore current is not atypical for other SiN_x pores where one can see a somewhat rocky background. $^{35-37}$

In Figure 2a the open pore current fluctuates by about 2% around the mean value and can be somewhat compensated for in the event analysis by allowing for a changing background current. Low frequency noise in ionic current for SiN_x nanopores has been empirically attributed to surface conditions or contamination. This noise may be pronounced here especially since we did not use piranha or other cleaning treatments prior to ionic measurements. In future studies, noise in these HF-etched SiN nanopores can be extensively characterized, similar to numerous studies with TEM-drilled pores. $^{35-37}$

The degree of current blockades by the DNA is an effective way to calibrate the pore size, given that DNA dynamics in SiN_x pores is well understood under these experimental conditions (1 M KCl).³³ Ionic conductance G through a single SiN_x nanopore can be analytically estimated with good accuracy^{18,33} as

$$G = \frac{I}{V} = \sigma \left(\frac{4t}{\pi d^2} + \frac{1}{d}\right)^{-1} \tag{1}$$

where d is the pore diameter, t is the membrane thickness, I is the open pore current, V is the applied voltage, and σ is the ionic solution conductivity ($\sigma \approx 12$ S/m for 1 M KCl at room temperature²⁸). The conductance change, ΔG , when the DNA blocks the pore is

$$\Delta G = \frac{\Delta I}{V} = \sigma \left\{ \left(\frac{4t}{\pi d^2} + \frac{1}{d} \right)^{-1} - \left[\frac{4t}{\pi (d^2 - d_{\text{DNA}}^2)} + \frac{1}{\sqrt{d^2 - d_{\text{DNA}}^2}} \right]^{-1} \right\}$$
 (2)

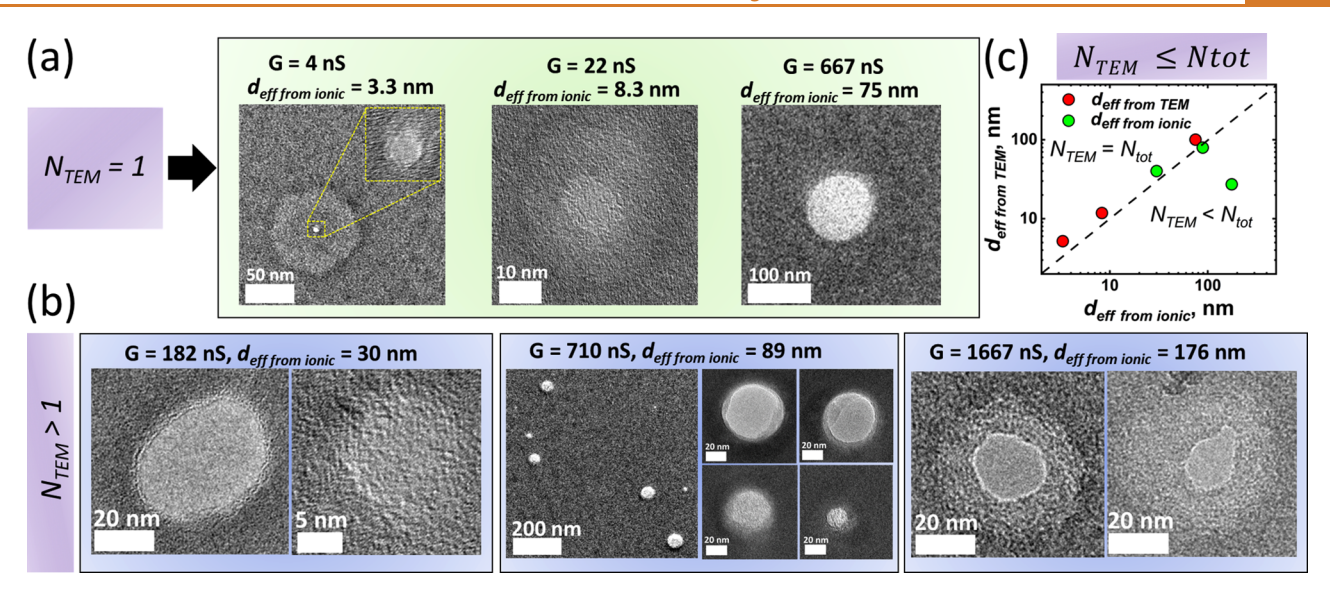


Figure 3. TEM images measured conductance G in 1 M KCl and estimated effective diameters $d_{\rm eff\ from\ ionic}$ for six glass chips. (a, top row) Only one pore $(N_{\rm TEM}=1)$ was located by TEM imaging. (b, bottom row) More than one pore (images showing $N_{\rm TEM}=2$, \sim 7, and 2 pores, respectively) were located by TEM imaging. (c) $d_{\rm eff\ from\ TEM}$ (eq 3) versus $d_{\rm eff\ from\ ionic}$ (eq 5) for the six chips shown. The individual pore diameters (used to calculate $d_{\rm eff\ from\ TEM}$ in (c)) extracted from TEM images using ImageJ are (a) 5.2 \pm 0.3 nm, 11.8 \pm 0.5 nm, 100.3 \pm 1.0 nm, from left to right, (b) 39.0 \pm 1.8 nm, 9.7 \pm 1.8 nm, left panel; 51.5 \pm 1.6 nm, 45.9 \pm 0.9 nm, 17.9 \pm 0.5 nm, and 35.2 \pm 0.6 nm, middle panel (clockwise from top left); 21.2 \pm 0.8 nm, 17.1 \pm 2.3 nm, right panel.

where ΔI is the current blockade by the DNA. These equations are used in the analysis below.

Figure 2a shows ionic measurements in 1 M KCl at 20 kHz across a membrane (G = 9.3 nS), corresponding to a calculated pore ("Pore 1") diameter of 4.8 nm assuming a 20 nm thick membrane (the expected thickness from SiN_x deposition). The size of Pore 1 was ideally suited for dsDNA translocations. Figure 2a shows current vs time after addition of 1 kbp dsDNA at V = +300 mV. DNA was purchased from ThermoFisher Scientific and measured at 10 nM concentration. To address if one or more pores formed, we quantitatively analyzed the DNA signals. The all-points histogram for the entire ionic current versus time trace shows three peaks: the baseline peak with a mean at 2.78 nA and standard deviation of 0.06 nA, a second peak corresponding to unfolded DNA events at 2.38 nA and standard deviation of 0.05 nA ($\langle \Delta I \rangle_{\rm DNA~unfolded} = 0.40$ ± 0.08 nA), and a smaller peak at 2.0 nA and standard deviation of 0.05 nA ($\langle \Delta I \rangle_{\rm DNA\ folded} = 0.78 \pm 0.08$ nA) corresponding to folded DNA signals. We detect only three types of events (Figure 2b). From the mean current blockade 0.40 ± 0.08 nA for unfolded DNA and the open pore current 2.78 ± 0.06 nA, using eqs 1 and 2 we calculate the pore diameter of 5.6 \pm 0.7 nm and effective thickness of 27.7 \pm 7.3 nm. These simple equations have been validated in numerous experiments with TEM-drilled and electroporated SiN pores. 15,18,39 Furthermore, the calculated pore diameter and thickness then predict the current depth from folded dsDNA to be 1.97 \pm 1.46 nA. Compared to the true measured value of 2.00 ± 0.05 nA, there is only 1.5% error between the means. The self-consistent agreement between the calculated G, ΔG (unfolded DNA), and ΔG (folded DNA) with the measured values provides evidence of single pore behavior, since the presence of additional pores would lead to larger mismatches between expected mean current depths of unfolded and folded events. Thus, if there are other pores, they contributed negligibly.

Furthermore, we used a different nanopore chip ("Pore 2" in Figure 2c,d) and performed additional DNA translocation measurements at higher bandwidths up to 200 kHz with the portable nanopore reader (Elements SRL, Italy) and additionally with another amplifier setup up to 10 MHz (Elements SRL, Italy, Figure S1 in Supporting Information). For data in Figure 2c,d we used the same 1 kbp dsDNA and same concentration of 10 nM. The effective diameter of Pore 2 was estimated to be \approx 4.5 nm assuming a membrane thickness of 20 nm, before being used for dsDNA translocation. The traces show visible events at 200 kHz and are further low pass filtered to a cutoff bandwidth of 20 kHz for event analysis (Figure 2c). Based on the open pore ionic current value, the pore expanded to an effective diameter of ≈13.1 nm during the measurement (G = 53.3 nS). Despite the background current change, we detected folded and unfolded dsDNA events. In the data set with V = +300 mV, the open pore current was about 11.0 nA and the data have been fit with a double Gaussian with the mean peak values of 11.00 nA and 10.45 nA ($\langle \Delta I \rangle_{\rm DNA~unfolded}$ = 0.55 nA). We also observed a small peak at approximately 10.08 nA ($\langle \Delta I \rangle_{\rm DNA~folded}$ = 9.92 nA). These mean values correspond to peaks in the all-point histogram of the current data and indicate two event populations. Examples of both populations are represented in the inset of Figure 2c by representative events, where both folded and unfolded dsDNA make up the two event populations. Furthermore, using eqs 1 and 2, we estimate the pore diameter to be 9.0 nm and membrane thickness to be 13.8 nm. We further calculated the current from folded dsDNA to be 9.89 nA. Compared to the measured folded dsDNA peak at 10.08 nA, there is a 1.9% between the mean values, again proving the likely presence of a single nanopore.

We then used the same chip and dsDNA sample and inserted the chip, after rinsing in DI water, into another setup capable of higher bandwidth up to 10 MHz. We ramped the voltage up to 1.6 V to increase the signal-to-noise ratio (SNR) and measured the open pore current of \approx 42 nA at 1.6 V in 1 M

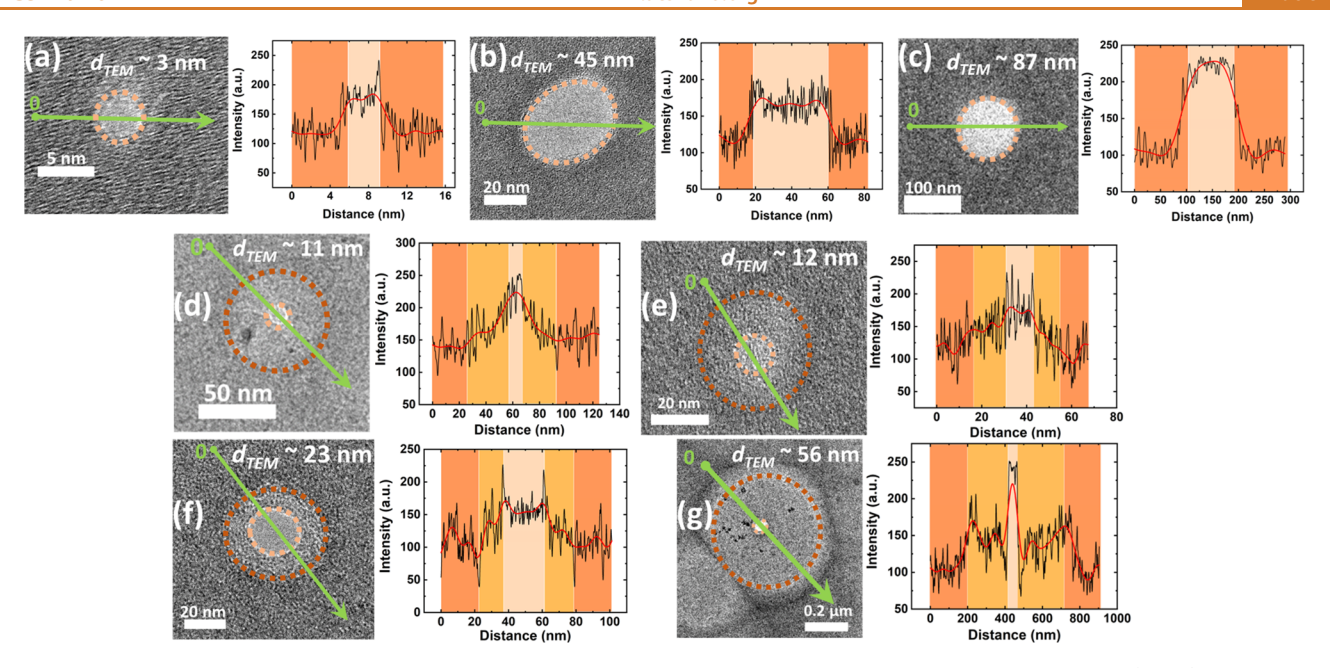


Figure 4. TEM images and corresponding TEM intensity cross sections of wet etched pores. TEM images and raw (black) and averaged (red) TEM intensity cross sections were taken along radial directions (green arrows) for seven pores with d_{TEM} indicated. Distances are measured from reference points indicated on the green arrows as "0". The pores (central parts) are mostly surrounded by sloped or flat (middle and bottom images) parts of the TEM intensity cross sections (dotted orange regions) corresponding to thinner membrane regions around the pores. These regions are located in TEM images within the orange circles. While the TEM signal contrast is not linearly proportional to thickness, 32 these TEM intensity cross sections nevertheless indicate thinner membrane areas surrounding some pores. The thinner regions are typically a few to 20 nm wide but can span up to \sim 300 nm (as in (g)).

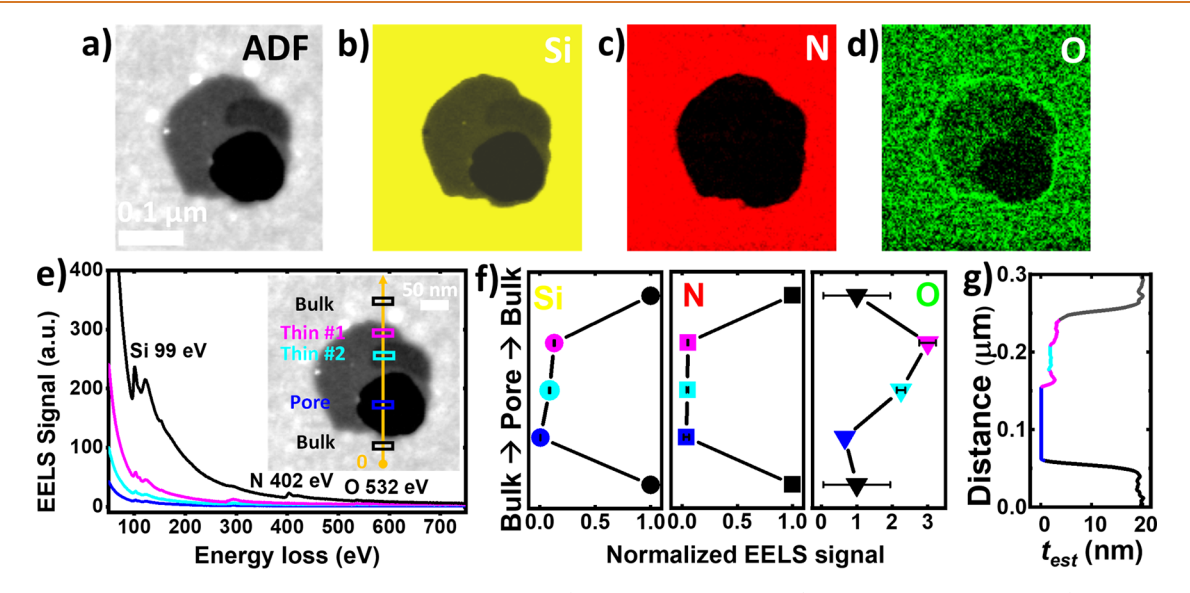


Figure 5. Example of HF-etched SiN_x nanopore with structural (annual dark field, ADF) and chemical structural (electron energy loss spectroscopy, EELS) characterization. (a) ADF images of a single nanopore. Two thinned regions around this pore were observed. (b-d) 2D EELS spatial intensity maps of the Si L (yellow), N K (red), and O K (green) edges at 99, 402, and 532 eV, respectively. (e) Representative EELS spectra taken across the nanopore, thinned regions, and unthinned bulk membrane region (corresponding ADF image shown as inset). (f) The Si L-edge, N K-edge, and O K-edge EELS signals at corresponding spatial positions were normalized by the highest magnitude in the bulk membrane. Standard error bars are from three nearby spatial positions. (g) Roughly estimated membrane thicknesses ($t_{\rm est}$) across the representative nanopore, thinned area, and surrounding membrane corresponding to the part e inset.

KCl. The calculated root-mean-square (rms) noise, $I_{\rm RMS}$ from this chip was 1.6 nA (Figure 2d), about 2 times smaller compared to a previous study at 10 MHz.^{7,40} Despite this improvement, translocation events were not readily observable due to insufficiently high SNR (Figure 2d) and require thinner SiN_x to increase SNR for successful detection.⁷

However, not all chips display a single pore behavior. Figure 3 features a subset of TEM images of pores on six glass chips created by etching, as well as the conductance *G* for those membranes. Images were obtained *after* the ionic measurements, and no cleaning processes besides rinsing in water were used. For some chips, a second ionic measurement was performed after TEM imaging. We observe the following based

on the TEM image contrast: more than 50% of pores studied formed within a thinned concentric region around the pore (lighter gray), whose width typically ranged from a few nm to about 20 nm but could span up to ~300 nm (dotted dark orange circles, Figure 4d-g). We do not have the experimental evidence to explain why this thin ring is more pronounced in some pores and less in others: not observing this ring in some pores could be partly a result from TEM imaging settings and experimental contrast, especially if the slope of the pore walls is not drastic and/or the membrane is thicker. For example, the thinned region surrounding the nanopore in Figure 5a is estimated to be as thin as $\approx 2-3$ nm and the low brightness contrast makes it challenging to distinguish the thinned area from the nanopore itself. Furthermore, this thinned region provides clues as to the mechanism of nanopore formation. It is likely that the formation of the pore is initiated in the thinner and/or defective area and gradually spreads throughout the whole SiN, window as the HF etching proceeds.

Figure 4 also shows TEM images and corresponding TEM intensity cross sections taken along radial directions for several nanopores. The thinned region is clearly visible in several examples and represented by the sloping or flat parts of the TEM intensity cross sections (dark orange regions, middle and bottom rows in Figure 4). In contrast, slopes in the top row figures (Figure 4a-c) are steeper (e.g., TEM intensity drops off approximately 50 au within 25 nm in Figure 4c). While the gray scale arbitrary units are not linearly proportional to membrane thickness,³² they nevertheless demarcate thinner regions around some pores. We observe some pores whose cross-sectional shapes appear as almost perfect circles. The wet HF etching is isotropic such that the etched region expands as a hemisphere through the membrane and the cross-section of the pore is expected to be a circle in the plane intersecting with the HF hemisphere droplet. The in-plane isotropic expansion can probably be larger than the initial droplet shape.

TEM images reveal either one (top row) or more pores (bottom row) (Figure 3). We used ImageJ to analyze TEM images. In some samples we located only one pore (Figure 3a) using TEM, and in others a few (Figure 3b), which can manifest itself in a higher conductance and as mismatch between the extracted parameters from eqs 1 and 2. From the open pore current alone, one cannot distinguish between one bigger pore or several smaller ones. TEM imaging, on the other hand, can miss pores in a membrane, especially if they are at low density. In contrast, it is easier to spot large pores (~100 nm) or clusters. TEM imaging may also erroneously imply that a membrane is pristine even if there is some pore present because it is challenging to inspect all membrane regions at high resolution (1 million images of area 100 nm × 100 nm would be required to image $100 \times 100 \ \mu m^{2}$ 41). While we attempted to locate all pores, some were likely missed, and thus $N_{\text{TEM}} \leq N_{\text{tot}}$. We define an effective pore diameter from TEM, $d_{\rm eff\ from\ TEM}$, as the diameter of a single pore whose area is equal to the sum of all pore areas from all available TEM images of that membrane:

$$d_{\rm eff\,from\,TEM} = \sqrt{\frac{4A_{\rm tot,TEM}}{\pi}} \tag{3}$$

Error in $d_{\rm eff\ from\ TEM}$ is the averaged difference between the mean diameter and the shortest and longest pore dimensions in the TEM image extracted by ImageJ. Similarly, ionic conductance G is an approximate measure of the total area

 $A_{
m tot,ionic}$ of all the pores. In Figure 3, G=4 nS to 1667 nS is calculated from the linear I-V curves in 1 M KCl for six membranes, with corresponding pore images identified by TEM inspection. Measurements were performed using a portable amplifier setup at 20 kHz 28 (Elements SRL, Italy). Assuming a total of $N_{
m tot}$ pores in parallel, we can estimate the total conductance G through the membrane to be on the order of

$$G = \sum_{i=1}^{N_{\text{tot}}} G_i = \sum_{i=1}^{N_{\text{tot}}} \frac{I_i}{V} = \sigma \sum_{i=1}^{N_{\text{tot}}} \left(\frac{4t_i}{\pi d_i^2} + \frac{1}{d_i} \right)^{-1}$$

$$\approx \sigma \sum_{i=1}^{N_{\text{tot}}} \frac{A_i}{t} = \sigma \frac{A_{\text{tot,ionic}}}{t} (t_i = t \gg d_i)$$
(4)

When pore thickness is significantly larger than pore diameter, $t_i \gg d_i$ (which is weakly satisfied here, membranes are ~20 and 100 nm thick, and observed pore diameters are generally smaller), we ignore the second term in the sum $(1/d_i)$ access resistance term) to simplify eq 4. G is then roughly proportional to the total porous area $A_{\text{tot,ionic}}$ (assuming all pores have the same thickness $t_i = t$). Noting these assumptions, we quote the *effective pore diameter* in Figure 3 from ionic measurements, $d_{\text{eff from ionic}}$:

$$d_{\rm eff\,from\,ionic} = \sqrt{\frac{4A_{\rm tot,ionic}}{\pi}} = \sqrt{\frac{4Gt}{\pi\sigma}} = 3.3 \text{ nm to } 176 \text{ nm}$$
(5)

From the measured G, we estimate the diameter $d_{\rm eff\ from\ ionic}$ of a single pore with the same conductance and thickness equal to the membrane thickness. This is useful to estimate the *maximum pore size* up to an order of magnitude. However, these assumptions are only approximately correct. Furthermore, for nearby pores, G is not the sum of individual conductances. In contrast, complementary TEM imaging can directly determine the pore number and diameter but requires fast scanning of large areas which is not well established.

Figure 3c shows $d_{\rm eff\ from\ TEM}$ (from eq 3) versus $d_{\rm eff\ from\ ionic}$ (from eq 5) reflecting the total nanoporous areas for membranes in Figure 3a,b. A line $d_{\text{eff from TEM}} = d_{\text{eff from ionic}}$ corresponds to $N_{\text{TEM}} = N_{\text{tot}}$. Most data points lie close to this line. For the outlier sample with the highest G, $N_{\rm TEM}$ < $N_{\rm tot}$, indicating that TEM missed some pores. The uncertainty in $N_{
m tot}$ presents challenges as in membrane electroporation. 15,39,42,43 The HF etching method here is an inherently stochastic process where pores likely form in the thinnest and/ or most defective regions. For example, in Figure 3b, thinner and brighter rims around the pore are observed (the bottom right images). Note that if pores are thinner than the membrane, $d_{\text{eff from ionic}}$ from eq 5 will be smaller. While electroporation is controlled by varying parameters¹⁵ (time, voltage, ion concentration, pH), here we control exposure time, volume of HF, ambient conditions, etc. This method could be refined by localizing etching via HF droplet localization or membrane prepatterning to localize pores in thinnest areas. Furthermore, we found that extensive HF etching induced multiple uneven etching areas across the whole SiN substrate surface (see Figure S2 in Supporting Information). TEM imaging and DNA translocations improve the accuracy with which the pore number and sizes are known and could be used to establish process parameters. Adjusting the membrane area to produce the expected pore number between 0 and 1 provides a path toward single pore

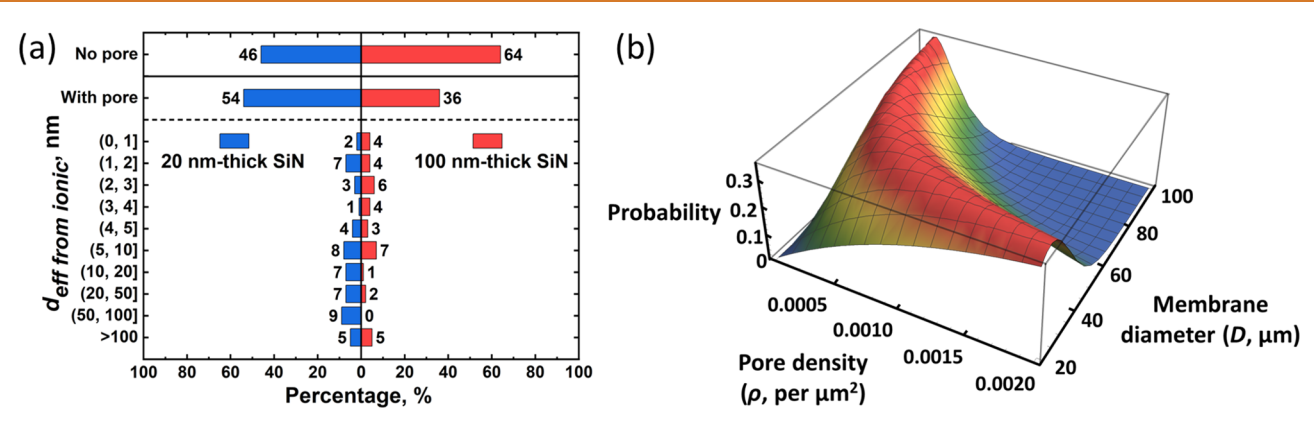


Figure 6. Statistics on 318 glass chips and probability estimates to find one or more pores per chip. (a) Percentage of glass chips by SiN membrane thickness (20 nm in blue and 100 nm in red) and by $d_{\rm eff \ from \ ionic}$ obtained by measuring conductance G across the SiN membranes in 1 M KCl. $d_{\rm eff \ from \ ionic}$ is estimated from eq 5 as described in the main text, assuming pore thicknesses are equal to the membrane thicknesses. Note that if pores are thinner, the estimated diameters from eq 5 in (a) would be smaller. (b) Calculated probability to find just one pore in a membrane vs pore density per area ρ (μ m²) and membrane diameter D (μ m). From ionic and TEM data we estimate $\rho = 5 \times 10^{-4}$ to 1×10^{-3} pores per μ m². For a fixed membrane diameter, D, the probability to find just one pore goes down with increasing D because the probability of finding *more* than one pore goes up.

membranes using large-scale HF etching. Our etching procedure produces zero, one, or a few pores (Figure 3). One way to decrease/increase $N_{\rm tot}$ in a probabilistic manner would be to decrease/increase the membrane size. Another way would be to modify the etching parameters and procedures, which will be explored in the future.

Beyond single pores per membrane, additional pores can contribute to the baseline conductance, although some may not fully wet and conduct. Assuming a known pore thickness, its diameter can be calculated from current blockades (eq 2). If this diameter is smaller than the diameter calculated from the open pore current (eq 1), this hints at the possible presence of other conducting channels. Conversely, if current blockades are consistent with DNA translocations through a single pore (Figure 2), this indicates with high confidence that there is only one pore. Additional pores that may not allow DNA translocation could increase the baseline current.³³

To further address the details of nanopore shape and composition, we used electron energy loss spectroscopy (EELS)^{18,32} in the aberration-corrected TEM (JEOL NEO-ARM S/TEM) to further examine the atomic structure and the underlying chemistry of the HF-etched pores. Figure 5a shows the annular dark-field (ADF) images of a representative pore with thinned areas. Around this pore we found lighter (thinned) membrane regions with different thicknesses around the nanopore, indicating localized thinned areas around the nanopore. Similar thinned areas around the nanopore were observed for TEM-drilled nanopores, 18 which was attributed to the Gaussian-like intensity profile of the TEM beam during TEM-based drilling. These findings indicate that regardless of the fabrication method, pores are likely to form in the thinned or defective regions on the membrane. We note that the thinned regions are also apparent in the 2D EELS maps (Figure 5b-d) as a function of their spatial positions. Both Si (yellow) and N (red) signals are the strongest on the unthinned bulk membrane (regions away from the pore) and gradually decay in the thinned region until reaching little to no signal inside the pore. This suggests that the thinned regions are both Si- and N-deficient compared to the unthinned membrane, with the removal of N at a greater extent.

In Figure 5e, we show the representative EELS spectra taken across the nanopore, thinned regions, and unthinned bulk

membrane. Furthermore, the Si L-edge, N K-edge, and O Kedge EELS signals at corresponding spatial positions were extracted and normalized by the highest magnitude in the bulk membrane, shown in Figure 5f. The Si signature signal is the lowest in the nanopore and slightly increased along the thinned regions. On the contrary, both the nanopore and thinned regions are significantly low in the N signature. Our observation is consistent with the largely N-deficient thin region, also previously reported for the TEM-drilled pores, and may indicate that the HF etching method in this work also results in a selectively greater removal of N from the membrane. A widespread signal from oxygen was seen across the nanopore and thinned area, which can be attributed to the formation of a native silicon oxide layer. 18 The aforementioned two thinned regions around the nanopore show different degrees of thinning, one ("Thin 2" in Figure 5e inset) thinner than the other ("Thin 1"). We performed further analysis and roughly estimated their thicknesses (t_{est} , Figure 5g) by extrapolating the intensity plot across the pore and membrane³² (Figure S3 in Supporting Information). The intensity plot across the nanopore shows that the membrane thickness was only slightly higher than the nanopore area (intensity of \approx 28 au and 34 au vs 14 au), which corresponds to a membrane only $\approx 2-3$ nm thick (Figure 5g). It is interesting and worth noting that the fluorine (F) EELS signal was also observed across the nanopore, thinned region, and unthinned bulk membrane (Figure S4 in Supporting Information). This indicates that a more intensive water rinse process than performed in this work may be required to completely remove residual fluorine from the HF etching process. Similarly, we saw EELS signals from K (purple) and Cl (aqua) across the samples (Figure S4 in Supporting Information), which we attributed to the residual KCl electrolyte after the currentvoltage (I-V) measurements used to estimate $d_{\text{eff from ionic}}$ after nanopore formation.

While silicon nitride is considered outstanding for its thermal and wear resistance, it is known to etch in aqueous HF. ⁴⁴ Upon HF contact with SiN_x, SiNH₂ groups are known to react with HF to eliminate NH₃ and form SiF₄ on the surface. In addition to membrane etching and thinning, we also occasionally noticed the presence of white cloudy dots close to the nanopore and thinned regions (see Figure S5 in Supporting

Information). The slightly lower Si and N signals in these dots, when compared with the unthinned bulk membrane away from the nanopore (normalized EELS signal Si 0.7 vs 1 and N 0.8 vs 1, respectively, see Figure S5), indicate that they are likely to be the precursor spots or intermediate products for any nanopore or thinning regions to form. We note that in refs 7 and 27 etching was terminated by removal of HF solution when it reaches the bottom of the SiN membrane and creates a spherical window. We added a set of optical microscope images in Figure S6 in Supporting Information to show the SiN membrane window exposure before, during, and after HF etching. In Figure S6D, we include a sketch and equation illustrating the etching process and how the membrane thickness is determined. The diameter of the etching spherical window, L, expands as $2 \times \sqrt{R^2 - t^2}$, where R is the radius of the bottom hemisphere and t is the thickness of the glass substrate as the etching proceeds. With a 49% HF solution used in the work, the etching rate is about 1 μ m/min.² Therefore, to ensure that the SiN membranes experience minimal HF exposure, the HF requires rapid removal.

Figure 6a shows the statistics from 318 chips by measuring G across the membranes in 1 M KCl. From G we calculated the diameter of an effective conductive pore, $d_{\text{eff from ionic}}$ (eq 5). These are upper bounds from eq 5 since we assume pores are as thick as the membrane. Figure 6a distinguishes the statistics grouped by membrane thickness (20 and 100 nm). For both thicknesses (same areas $\sim 2000 \ \mu \text{m}^2$) we obtain membranes with no pores and with one (or a few) pore(s) (see also Figure 3). G per unit area ranges from 0 (no pores) to 0.2 pS/ μ m² $(N_{\rm tot}$ = 1) and up to 850 pS/ $\mu{\rm m}^2$ $(N_{\rm tot} > 1)$. Additional TEM imaging of seven control membranes on Si chips yielded pores with diameters from 1.8 to 26 nm (average 10.6 nm). Furthermore, in Figure 6a we see that roughly about 1/2 of all chips had no nanopore, while 25-28% of all chips (per fixed membrane thickness, Figure 6a) had effective pore diameters of <10 nm, which means the membranes had only one pore that is of that size or several much smaller pores with the same total area. This corresponds to 80–90 chips (out of 318) likely usable for DNA translocation measurements. In contrast, 5-14% of all chips had effective pore diameters 50 nm or larger.

The probability of finding just one pore per membrane as a function of pore density, ρ , and membrane diameter, D, is calculated in Figure 6b. From ionic and TEM data, $\rho = 5 \times$ 10^{-4} to 1×10^{-3} pores/ μ m². Assuming this density, the expected pore number is $N = \rho \pi (D/2)^2$ (for $D = 50 \mu m$ and N= 1, $\rho = 5 \times 10^{-4}$ pores/ μ m²). For a stochastic process, the probability Pr[k,N] of finding k pores can be calculated with the generating function: $Pr[k,N] = N^k e^{-N}/k!$, where k is the number of pores and N is the expected value. For D = 50 μ m, the probabilities to find $N_{\text{tot}} = 0$, 1, 2, and 3 pores per membrane are \sim 0.37, 0.37, 0.18, and 0.06, respectively. This is roughly consistent with our statistical result on total pore formation percentages (Figure 6a, 54% for 20 nm thick, and 36% for 100 nm thick SiN). One benefit of this method is that it is inexpensive and quick: large numbers of nanopore chips can be fabricated quickly (hundreds of chips per 4 in. wafer). While etching is a stochastic process and nanopore control in this work remains to be further developed, chips can be quickly sorted out by effective conductance and estimated diameters as shown in Figure 6a and used for different studies and applications with some probabilistic success rate.

In the future, this method could be refined by spatially confining etching via HF droplet localization or membrane prepatterning to localize pores in the thinnest areas. Adjusting the membrane area to produce the expected pore number between 0 and 1 provides a path toward single pore membranes using large-scale HF etching. Furthermore, one could try to improve control over nanopore size and number by changing the HF concentration, by intentionally including various defect types in the membrane, by controlling temperature, and possibly via other means.

CONCLUSIONS

We demonstrated DNA translocations through SiN_x pores made by HF etching and their initial characterization. This microscopic etching and pore formation is a phenomenon that occurs in a probabilistic manner. The etched pores are suitable for ionic and translocation measurements, as confirmed by direct TEM imaging, ionic measurements, and dsDNA translocations. Given the simplicity of the etching process, the results and data analysis presented are attractive for applications of nanopores and nanoporous membranes and can be optimized for specific requirements. This method can produce heterogeneous nanopore size distributions, as well as occasionally multiple pores on the same membrane, often without sufficient control of their number. In a significant number of cases, we see the formation of single nanopores per membrane as shown in Figure 3, verified by combined TEM, ionic current, and successful DNA translocations. About 25-28% of all chips (per fixed membrane thickness, Figure 6a) had effective pore diameters of <10 nm. Thicker membranes gave fewer pores (36% of thicker membranes had pores vs 54% for thinner ones). The approach of nanopore fabrication is easy and adaptable for future single molecule sensing but requires additional work to improve control over the size and number of pores per membrane, as well as the yield of successful nanopores formation. Furthermore, it is interesting to compare the stability and lifetime of HF-etched pores compared to the typical TEM-drilled pores. From our experimental experience so far, we do not notice empirically any significant difference in stability or lifetime of these HF-etched pores compared to regular, TEM-drilled pores. We were able to get ionic conduction and DNA translocations through these nanopores several months after the chips were fabricated.

Nanopores are valuable in ion detection, filtration, and molecule analysis, and ionic conductance should be concordant with TEM-measured pore sizes. Future studies of pore formation mechanisms, pore shape, and composition could include *in situ* liquid TEM⁴⁵ to monitor pore formation in real time, TEM tomography^{32,46} to map their 3D shape. This HF etching process is the industrial-scale process that makes solid-state nanopores more accessible for a wide variety of biomedical applications including DNA, protein and biomarker sensing, water contaminant monitoring, blue energy harvesting, and many others.

MATERIALS AND METHODS

Nanopore Fabrication. Nanopores were fabricated in 20 nm and 100 nm thick low-stress SiN_x membrane suspended on 250 μ m thick, 5 × 5 mm² low-noise glass chips (Goeppert LLC, PA). The pores are fabricated following the procedure illustrated in Figure 1. Briefly, 0.5 μ L of 49% HF was administered to individual chips in a consecutive way for 5 s and then aspirated with a pipette. Five microliters of DI water was used to rinse each chip three times. The

chips were then left to air-dry after aspiration of the DI water and transported for further TEM imaging and ionic current characterizations and translocation measurements to characterize pore formation and properties. All chips were characterized by ionic measurements first, and then a fraction of them were imaged by TEM after the ionic measurements.

TEM Imaging. Chips after HF etching were imaged with a 200 keV focused electron beam in a JEOL 2010F transmission electron microscope (TEM). The diameters of the nanopore, $d_{\rm TEM}$, were measured by TEM imaging in vacuum. The error in diameter measurement from these images using ImageJ is about 0.3 to 2.3 nm.

lonic Current and DNA Translocation Measurements. Ionic measurements at bandwidths of 20 kHz and 200 kHz were performed using the portable Nanopore reader 200 kHz (Elements SRL, Italy). The measurements at a higher bandwidth of up to 10 MHz were collected with the 10 MHz Nanopore reader (Elements SRL, Italy) (Figure S1 in Supporting Information) and corresponding fluidic cell. All measurements were conducted in unbuffered 1 M KCl. DNA samples were 1 kbp dsDNA purchased from ThermoFisher Scientific (ThermoFisher Scientific, MA) and diluted to 10 nM in unbuffered 1 M KCl. Data were analyzed using custom-made programs in MATLAB (MathWorks, MA) and OriginLab (OriginLab, MA).

Annular Dark Field (ADF) TEM Imaging and Electron Energy Loss Spectroscopy (EELS) Measurements. Dark-field images were collected on the JEOL NEOARM operating at 200 kV with a high-angle annular dark filed (HAADF) detector. EELS spectra and elemental maps were acquired using the GIF Quantum Summit detector with an energy dispersion of 0.5 eV/channel. The EELS maps were collected with an exposure time of 0.02 s/pixel and the elemental quantification was done using DigitalMicrograph.

ASSOCIATED CONTENT

Supporting Information

The Supporting Information is available free of charge at https://pubs.acs.org/doi/10.1021/acsnano.2c07240.

Additional experimental information on the nanopore readers and fluidic cells, TEM images of nanopores after extensive HF etching, 2D EELS images on additional elemental compositions of nanopore in Figure 6a, structural (ADF) and chemical structural (EELS) characterization of white cloudy dots close to the nanopore and surrounding thinned areas, and optical microscope images of the glass chip at various processing stages, before, during, and right after the HF etching (PDF)

AUTHOR INFORMATION

Corresponding Authors

Zehui Xia – Goeppert LLC, Philadelphia, Pennsylvania 19146, United States; Email: zx@gppert.com

Marija Drndić — Department of Physics and Astronomy, University of Pennsylvania, Philadelphia, Pennsylvania 19104, United States; orcid.org/0000-0002-8104-2231; Email: drndic@physics.upenn.edu

Authors

Andre Scott – Goeppert LLC, Philadelphia, Pennsylvania 19146, United States

Rachael Keneipp – Department of Physics and Astronomy, University of Pennsylvania, Philadelphia, Pennsylvania 19104, United States

Joshua Chen — Department of Physics and Astronomy and Department of Materials Science and Engineering, University of Pennsylvania, Philadelphia, Pennsylvania 19104, United States David J. Niedzwiecki – Goeppert LLC, Philadelphia, Pennsylvania 19146, United States

Brian DiPaolo – Goeppert LLC, Philadelphia, Pennsylvania 19146, United States

Complete contact information is available at: https://pubs.acs.org/10.1021/acsnano.2c07240

Author Contributions

A.S, D.J.N., and Z.X. conceived the experiments, developed the fabrication protocols, and performed ionic testing. A.S. and Z.X. performed DNA translocation measurements. R.K. performed the EELS imaging and analysis. J.C. and M.D. helped with TEM, ionic, and DNA translocation analysis. Z.X. performed TEM imaging and image analysis. All authors discussed the manuscript and contributed throughout the writing process.

Notes

The authors declare the following competing financial interest(s): M.D. is a founder and consultant of Goeppert (www.gppert.com) that manufactures nanotechnology products including nanopore chips, fluid cells, and TEM supplies.

ACKNOWLEDGMENTS

The chips were fabricated at the Pennovation Center, the Singh Center for Nanotechnology, and at Rutgers University by Goeppert LLC. The work was supported NASA SBIR Phase II Grant 80NSSC19C0171. The Singh Center is supported by the NSF Grant NNCI-1542153. We acknowledge the use of JEOL 2010F TEM at Rutgers University. M.D. and R.K. acknowledge the use of AC-TEM instrumentation supported by the NSF through the University of Pennsylvania Materials Research Science and Engineering Center (MRSEC) Grant DMR-1720530. We thank Prof. V. Tabard-Cossa for sharing I-V curves, and Prof. A. Radenovic for sharing TEM images.

REFERENCES

- (1) Drndic, M. 20 Years of Solid-State Nanopores. *Nat. Rev. Phys.* **2021**, 3 (9), 606–606.
- (2) Li, J.; Stein, D.; McMullan, C.; Branton, D.; Aziz, M. J.; Golovchenko, J. A. Ion-Beam Sculpting at Nanometre Length Scales. *Nature* **2001**, *412*, 166–169.
- (3) Xue, L.; Yamazaki, H.; Ren, R.; Wanunu, M.; Ivanov, A. P.; Edel, J. B. Solid-State Nanopore Sensors. *Nat. Rev. Mater.* **2020**, *5* (12), 931–951.
- (4) Storm, A. J.; Chen, J. H.; Ling, X. S.; Zandbergen, H. W.; Dekker, C. Fabrication of Solid-State Nanopores with Single-Nanometre Precision. *Nat. Mater.* **2003**, *2* (8), 537–540.
- (5) Rosenstein, J. K.; Wanunu, M.; Merchant, C. A.; Drndic, M.; Shepard, K. L. Integrated Nanopore Sensing Platform with Sub-Microsecond Temporal Resolution. *Nat. Methods* **2012**, *9* (5), 487–492.
- (6) Wanunu, M.; Meller, A. Chemically Modified Solid-State Nanopores. *Nano Lett.* **2007**, *7* (6), 1580–1585.
- (7) Chien, C.-C.; Shekar, S.; Niedzwiecki, D. J.; Shepard, K. L.; Drndić, M. Single-Stranded DNA Translocation Recordings through Solid-State Nanopores on Glass Chips at 10 MHz Measurement Bandwidth. *ACS Nano* **2019**, *13* (9), 10545–10554.
- (8) Klein, O.; Biskupek, J.; Forghani, K.; Scholz, F.; Kaiser, U. TEM Investigations on Growth Interrupted Samples for the Correlation of the Dislocation Propagation and Growth Mode Variations in AlGaN Deposited on SiNx Interlayers. *J. Cryst. Growth* **2011**, 324 (1), 63–72.
- (9) Westenfelder, B.; Meyer, J. C.; Biskupek, J.; Algara-Siller, G.; Lechner, L. G.; Kusterer, J.; Kaiser, U.; Krill, C. E.; Kohn, E.; Scholz, F. Graphene-Based Sample Supports Forin Situhigh-Resolution TEM Electrical Investigations. *J. Phys. D: Appl. Phys.* **2011**, 44 (5), 055502.

- (10) Bogan, M. J.; Henry Benner, W.; Hau-Riege, S. P.; Chapman, H. N.; Frank, M. Aerosol Sample Preparation Methods for X-Ray Diffractive Imaging: Size-Selected Spherical Nanoparticles on Silicon Nitride Foils. *J. Aerosol Sci.* **2007**, *38* (11), 1119–1128.
- (11) Venta, K.; Shemer, G.; Puster, M.; Rodríguez-Manzo, J. A.; Balan, A.; Rosenstein, J. K.; Shepard, K.; Drndić, M. Differentiation of Short, Single-Stranded DNA Homopolymers in Solid-State Nanopores. *ACS Nano* **2013**, *7* (5), 4629–4636.
- (12) Tong, H. D.; Jansen, H. V.; Gadgil, V. J.; Bostan, C. G.; Berenschot, E.; van Rijn, C. J. M.; Elwenspoek, M. Silicon Nitride Nanosieve Membrane. *Nano Lett.* **2004**, *4* (2), 283–287.
- (13) Fischbein, M. D.; Drndić, M. Sub-10 Nm Device Fabrication in a Transmission Electron Microscope. *Nano Lett.* **2007**, *7* (5), 1329–1337
- (14) Wanunu, M.; Dadosh, T.; Ray, V.; Jin, J.; McReynolds, L.; Drndić, M. Rapid Electronic Detection of Probe-Specific MicroRNAs Using Thin Nanopore Sensors. *Nat. Nanotechnol.* **2010**, 5 (11), 807–814.
- (15) Waugh, M.; Briggs, K.; Gunn, D.; Gibeault, M.; King, S.; Ingram, Q.; Jimenez, A. M.; Berryman, S.; Lomovtsev, D.; Andrzejewski, L.; Tabard-Cossa, V. Solid-State Nanopore Fabrication by Automated Controlled Breakdown. *Nat. Protoc.* **2020**, *15* (1), 122–143.
- (16) Zvuloni, E.; Zrehen, A.; Gilboa, T.; Meller, A. Fast and Deterministic Fabrication of Sub-5 Nanometer Solid-State Pores by Feedback-Controlled Laser Processing. *ACS Nano* **2021**, *15* (7), 12189–12200.
- (17) Gilboa, T.; Zvuloni, E.; Zrehen, A.; Squires, A. H.; Meller, A. Automated, Ultra-Fast Laser-Drilling of Nanometer Scale Pores and Nanopore Arrays in Aqueous Solutions. *Adv. Funct. Mater.* **2020**, *30*, 1900642.
- (18) Chou, Y.-C.; Masih Das, P.; Monos, D. S.; Drndić, M. Lifetime and Stability of Silicon Nitride Nanopores and Nanopore Arrays for Ionic Measurements. *ACS Nano* **2020**, *14* (6), 6715–6728.
- (19) Ring, E. A.; Peckys, D. B.; Dukes, M. J.; Baudoin, J. P.; De Jonge, N. Silicon Nitride Windows for Electron Microscopy of Whole Cells. J. Microsc. 2011, 243 (3), 273–283.
- (20) Bocquet, L.; Charlaix, E. Nanofluidics, from Bulk to Interfaces. *Chem. Soc. Rev.* **2010**, 39 (3), 1073–1095.
- (21) Haywood, D. G.; Saha-Shah, A.; Baker, L. A.; Jacobson, S. C. Fundamental Studies of Nanofluidics: Nanopores, Nanochannels, and Nanopipets. *Anal. Chem.* **2015**, *87* (1), 172–187.
- (22) Alexander, K.; George, J. P.; Verbist, J.; Neyts, K.; Kuyken, B.; Van Thourhout, D.; Beeckman, J. Nanophotonic Pockels Modulators on a Silicon Nitride Platform. *Nat. Commun.* **2018**, *9* (1), 3444.
- (23) Dhakal, A.; Subramanian, A. Z.; Wuytens, P.; Peyskens, F.; Thomas, N. L.; Baets, R. Evanescent Excitation and Collection of Spontaneous Raman Spectra Using Silicon Nitride Nanophotonic Waveguides. *Opt. Lett.* **2014**, *39* (13), 4025–4028.
- (24) Sharma, N.; Hooda, M.; Sharma, S. K. Synthesis and Characterization of LPCVD Polysilicon and Silicon Nitride Thin Films for MEMS Applications. *J. Mater.* **2014**, 2014, 954618.
- (25) Zaghloul, U.; Papaioannou, G.; Coccetti, F.; Pons, P.; Plana, R. Dielectric Charging in Silicon Nitride Films for MEMS Capacitive Switches: Effect of Film Thickness and Deposition Conditions. *Microelectron. Reliab.* **2009**, 49 (9), 1309–1314.
- (26) Fried, J. P.; Swett, J. L.; Nadappuram, B. P.; Mol, J. A.; Edel, J. B.; Ivanov, A. P.; Yates, J. R. In Situ Solid-State Nanopore Fabrication. *Chem. Soc. Rev.* **2021**, *50* (8), 4974–4992.
- (27) Balan, A.; Chien, C.-C.; Engelke, R.; Drndić, M. Suspended Solid-State Membranes on Glass Chips with Sub 1-PF Capacitance for Biomolecule Sensing Applications. *Sci. Rep.* **2016**, 5 (1), 17775.
- (28) Niedzwiecki, D. J.; Chou, Y.-C.; Xia, Z.; Thei, F.; Drndić, M. Detection of Single Analyte and Environmental Samples with Silicon Nitride Nanopores: Antarctic Dirt Particulates and DNA in Artificial Seawater. *Rev. Sci. Instrum.* **2020**, *91* (3), 031301.
- (29) Xia, Z.; Lin, C.-Y.; Drndić, M. Protein-Enabled Detection of Ibuprofen and Sulfamethoxazole Using Solid-State Nanopores. *Proteomics* **2022**, 22 (5–6), 2100071.

- (30) Balan, A.; Drndic, M. Ultra Low Capacitance Glass Supported Dielectric Membranes for Macromolecular Analysis. US10274478, April 30, 2019.
- (31) Fischbein, M. D.; Drndić, M. Nanogaps by Direct Lithography for High-Resolution Imaging and Electronic Characterization of Nanostructures. *Appl. Phys. Lett.* **2006**, 88 (6), 063116.
- (32) Rodríguez-Manzo, J. A.; Puster, M.; Nicolaï, A.; Meunier, V.; Drndić, M. DNA Translocation in Nanometer Thick Silicon Nanopores. *ACS Nano* **2015**, *9* (6), 6555–6564.
- (33) Chou, Y.-C.; Chen, J.; Lin, C.-Y.; Drndić, M. Engineering Adjustable Two-Pore Devices for Parallel Ion Transport and DNA Translocations. J. Chem. Phys. 2021, 154 (10), 105102.
- (34) Healy, K.; Ray, V.; Willis, L. J.; Peterman, N.; Bartel, J.; Drndić, M. Fabrication and Characterization of Nanopores with Insulated Transverse Nanoelectrodes for DNA Sensing in Salt Solution. *Electrophoresis* **2012**, *33* (23), 3488–3496.
- (35) Fragasso, A.; Pud, S.; Dekker, C. 1/f Noise in Solid-State Nanopores Is Governed by Access and Surface Regions. *Nanotechnology* **2019**, *30* (39), 395202.
- (36) Fragasso, A.; Schmid, S.; Dekker, C. Comparing Current Noise in Biological and Solid-State Nanopores. *ACS Nano* **2020**, *14* (2), 1338–1349.
- (37) Smeets, R. M. M.; Keyser, U. F.; Dekker, N. H.; Dekker, C. Noise in Solid-State Nanopores. *Proc. Natl. Acad. Sci. U. S. A.* **2008**, 105 (2), 417–421.
- (38) Merchant, C. A.; Healy, K.; Wanunu, M.; Ray, V.; Peterman, N.; Bartel, J.; Fischbein, M. D.; Venta, K.; Luo, Z.; Johnson, A. T. C.; Drndić, M. DNA Translocation through Graphene Nanopores. *Nano Lett.* **2010**, *10* (8), 2915–2921.
- (39) Kwok, H.; Briggs, K.; Tabard-Cossa, V. Nanopore Fabrication by Controlled Dielectric Breakdown. *PLoS One* **2014**, *9* (3), e92880.
- (40) Shekar, S.; Niedzwiecki, D. J.; Chien, C.-C.; Ong, P.; Fleischer, D. A.; Lin, J.; Rosenstein, J. K.; Drndić, M.; Shepard, K. L. Measurement of DNA Translocation Dynamics in a Solid-State Nanopore at 100 Ns Temporal Resolution. *Nano Lett.* **2016**, *16* (7), 4483–4489.
- (41) Chen, J.; Balan, A.; Masih Das, P.; Thiruraman, J. P.; Drndić, M. Computer Vision AC-STEM Automated Image Analysis for 2D Nanopore Applications. *Ultramicroscopy* **2021**, 231, 113249.
- (42) Carlsen, A. T.; Briggs, K.; Hall, A. R.; Tabard-Cossa, V. Solid-State Nanopore Localization by Controlled Breakdown of Selectively Thinned Membranes. *Nanotechnology* **2017**, *28* (8), 085304.
- (43) Leung, C.; Briggs, K.; Laberge, M.-P.; Peng, S.; Waugh, M.; Tabard-Cossa, V. Mechanisms of Solid-State Nanopore Enlargement under Electrical Stress. *Nanotechnology* **2020**, *31* (44), 44LT01.
- (44) Martin Knotter, D.; Denteneer, T. J. J. Etching Mechanism of Silicon Nitride in HF-Based Solutions. *J. Electrochem. Soc.* **2001**, *148* (3), F43.
- (45) Wu, J.; Shan, H.; Chen, W.; Gu, X.; Tao, P.; Song, C.; Shang, W.; Deng, T. In Situ Environmental TEM in Imaging Gas and Liquid Phase Chemical Reactions for Materials Research. *Adv. Mater.* **2016**, 28 (44), 9686–9712.
- (46) Kim, M. J.; McNally, B.; Murata, K.; Meller, A. Characteristics of Solid-State Nanometre Pores Fabricated Using a Transmission Electron Microscope. *Nanotechnology* **2007**, *18* (20), 205302.
- (47) Xia, Z.; Patchin, M.; McKay, C. P.; Drndic, M. Deoxyribonucleic Acid Extraction from Mars Analog Soils and Their Characterization with Solid-State Nanopores. *Astrobiology* **2022**, *22*, 992.